Correlation analysis of three-dimensional strain imaging using ultrasound two-dimensional array transducers

Min Rao[a] and Tomy Varghese
Department of Medical Physics, The University of Wisconsin-Madison, 1300 University Avenue, 1530 MSC, Madison, Wisconsin 53706

(Received 24 January 2008; revised 4 June 2008; accepted 5 June 2008)

Two-dimensional (2D) transducer arrays represent a promising solution for implementing real time three-dimensional (3D) ultrasound elastography. 2D arrays enable electronic steering and focusing of ultrasound beams throughout a 3D volume along with improved slice thickness performance when compared to one-dimensional (1D) transducer arrays. Therefore, signal decorrelation caused by tissue motion in the elevational (out-of-plane) direction needs to be considered. In this paper, a closed form expression is derived for the correlation coefficient between pre- and postdeformation ultrasonic radio frequency signals. Signal decorrelation due to 3D motion of scatterers within the ultrasonic beam has been considered. Computer simulations are performed to corroborate the theoretical results. Strain images of a spherical inclusion phantom generated using 1D and 2D array transducers are obtained using a frequency domain simulation model. Quantitative image quality parameters, such as the signal-to-noise and contrast-to-noise ratios obtained using 1D, 2D, and 3D motion tracking algorithms, are compared to evaluate the performance with the 3D strain imaging system. The effect of the aperture size for 2D arrays and other factors that affect signal decorrelation are also discussed. [DOI: 10.1121/1.2953310]

PACS number(s): 43.80.Qf [FD] Pages: 1858–1865

I. INTRODUCTION

Elastography is an imaging modality that is based on mapping local internal strains that tissues experience after a quasistatic or dynamic deformation.[1–3] Until recently, most studies devoted to elastography were focused on the estimation of the axial component of the strain. However, motion in tissue occurs in three dimensions and is coupled with each other when subjected to an axial compression or deformation. Although the third component of the displacement vector can be obtained from two-dimensional (2D) motion estimation by using the assumption of incompressibility, 2D motion tracking may suffer from decorrelation noise caused by out-of-plane tissue movement in the elevational direction. In addition, the incompressibility assumption may not hold in some tissues,[1,2] leading to errors. In addition, the Poisson's ratio may not be constant, such as for poroelastic tissue when edema is present.[3,4] Therefore, all the components of the strain tensor and displacement vector are required to characterize the resulting deformation.[5,6] Because the components of the strain tensor are coupled, accurate estimations of all components are necessary for a complete visualization of the strain incurred in tissue. Without those components, other important parameters such as shear strains cannot be estimated. In addition, knowledge of all the strain tensor components leads to an accurate Young's modulus reconstruction of the underlying tissue elasticity.[7,8]

To estimate displacement vectors and strain tensors in all three dimensions, three-dimensional (3D) volume data are required. 2D transducer arrays represent a promising solution for implementing real time 3D data acquisition. 2D arrays provide the capability for electronic steering and focusing of ultrasound beams throughout a 3D volume. Thus, they have improved slice thickness attributes when compared to one-dimensional (1D) and multirow transducer arrays. A problem facing the development of 2D arrays is the complexity arising from the large number of array elements required in such transducers and the channel capacity needed for the ultrasound system. Because of the complexity of implementing 2D array systems, it is particularly important to develop theoretical models to evaluate the performance and tradeoffs of strain imaging obtained with 2D arrays and to determine optimum parameters for these systems.

Previous works on 3D strain imaging have been reported in the literature.[9–13] Promising 3D strain imaging results have been demonstrated using 1D arrays with mechanical translation in the elevational direction utilized to acquire multiple B-scans followed by reconstruction to create the 3D image.[10,12] Konofagou and Ophir[9] described a 3D motion tracking algorithm and presented simulated strain images obtained using 1.5D and 2D array transducers. In that work, however, the simulated pre- and postdeformation ultrasonic radio frequency (rf) signals were obtained through a convolution of the point-spread function (PSF) with a tissue scattering function, where the 3D beam forming procedure with a 2D array was not simulated. Awad and Yen[11] also described a 3D strain imaging system using a prototype rectilinear sparse 2D array. However, thus far the performance of 3D strain imaging systems using fully sampled 2D arrays has not been thoroughly investigated.

Signal decorrelation noise is one of the major limiting factors in strain estimation and imaging.[8,9] The normalized

[a]Electronic mail: minrao@wisc.edu

correlation coefficient has been utilized previously to ascertain the degree of signal decorrelation and to quantify the accuracy and precision of strain estimates. A large amount of theoretical derivations has been reported in the literature to calculate the correlation coefficient between the pre- and postdeformation rf signals.[4,5,10–12] In most of these publications, 2D models were utilized since ultrasound beams with 1D array transducers are significantly wider in the elevational direction when compared to the lateral direction. Thus, scatterer movement in the elevational direction did not cause a significant loss of coherence in the echoes. In the case of 2D arrays, however, the out-of-plane motion (in the elevational direction) needs to be considered since the beam width is similar in both the lateral and elevational directions. Therefore, a 3D model is required to evaluate signal decorrelation due to the 3D motion. Kallel and Ophir[5] proposed a 3D model for predicting the correlation coefficient using separable point-spread functions in the axial, lateral, and elevational directions. In that work, the expression for the correlation coefficient was derived under the assumption that the lateral and elevational components of displacement are constant within the ultrasound beam. In practice, tissue scatterers move relative to each other in 3D space due to the applied compression or deformation. Thus the resulting signal decorrelation is caused by tissue distortion in all three dimensions. Therefore, the assumption of a simple translation of tissue scatterers in the lateral and elevational directions during compression is not valid and may result in a biased estimation of the correlation coefficient.

In this paper, a closed form theoretical expression is derived for the correlation coefficient between pre- and postdeformation ultrasonic rf signals. Signal decorrelation due to the 3D motion of scatterers within the ultrasonic beam has been considered. To corroborate the theoretical development, ultrasound (US) simulations using 1D and 2D arrays are performed and the results of a simulated uniformly elastic phantom, which verify the theoretical expression, are presented. Factors that affect signal decorrelation are discussed. Another purpose of this study is to present strain images from a simulated spherical inclusion phantom obtained using 1D and 2D arrays with different aperture sizes. Modern 3D beam forming techniques with 2D array transducers, such as dynamic aperture and dynamic receive focusing, have been implemented in our simulation.

II. THEORY

Ultrasonic rf echo signals before and after the applied deformation is modeled using

$$s_1 = P(x,y,z) \otimes T(x,y,z),$$

$$s_2 = P(x,y,z) \otimes T(x/b, y/b, z/a), \tag{1}$$

where subscripts 1 and 2 denote pre- and postdeformation echo signals obtained from an elastic tissue medium, and x, y, and z are the lateral, elevational, and axial coordinates, respectively, $T(x,y,z)$ denotes the tissue scattering function, and $P(x,y,z)$ is the pulse-echo PSF of the imaging system. The symbol $\otimes$ denotes the convolution operation. The parameters a and b denote the compression or expansion factor that scales the tissue scattering function defined in terms of the actual applied tissue strain ε

$$a = 1 - \varepsilon, \quad b = 1 + \frac{\varepsilon}{\nu}, \tag{2}$$

where ν is the Poisson ratio. There are several models that define the $T(x,y,z)$ term. To simplify the tissue model, we assume a large number of very small inhomogeneities (Rayleigh scatterers) with respect to the wavelength of the PSF,[14]

$$T(x,y,z) = \sum_i T_i \delta(x - x_i, y - y_i, z - z_i), \tag{3}$$

where $\delta(x,y,z)$ is the 3D Dirac or impulse function, (x_i, y_i, z_i) denote the randomly distributed centers of each inhomogeneity, and T_i represents the echogenicity of each scatterer. The scatterer distribution is assumed to be δ correlated, which means the correlation length of scatterers is very short compared to the acoustic wavelength of the transmit pulse.

The cross correlation between the signals acquired before and after deformation can be written as[15]

$$\langle s_1 s_2^* \rangle = \int\int\int P(l_{1x}, l_{1y}, l_{1z}) P(l_{2x}, l_{2y}, l_{2z}) \exp(j\Delta\phi) dx dy dz, \tag{4}$$

where $\Delta\phi$ is the phase difference between pre- and postdeformation signals, which can be written as $\Delta\phi = 4\pi(R_2 - R_1)/\lambda$, where λ is the wavelength at the center frequency, and R_1 and R_2 are the distances from the scatterer to the transducer for the pre- and postdeformation situations, respectively,

$$R_1 = \sqrt{(x - x_0)^2 + (y - y_0)^2 + z^2},$$

$$R_2 = \sqrt{(bx - x_0)^2 + (by - y_0)^2 + (az)^2}. \tag{5}$$

Under the assumption that the depth of interest z_{01} is much larger than the beam width, we obtain

$$R_2 - R_1 \approx \frac{(b^2-1)x^2 - 2(b-1)x_0 x + (b^2-1)y^2 - 2(b-1)y_0 y + (a^2-1)z^2}{2z_{01}}. \tag{6}$$

Here we assume that the 3D PSF is separable in three dimensions, an assumption that holds at the focus,[16] We can write $P(x,y,z)$ as

$$P(x,y,z) = p_x(x)p_y(y)p_z(z). \tag{7}$$

The axial, lateral, and elevational PSF components may be modeled as Gaussian envelopes with characteristic widths σ_z, σ_x, and σ_y, respectively,[17]

$$p_z(z) = \exp(-z^2/2\sigma_z^2), \quad p_x(x) = \exp(-x^2/2\sigma_x^2),$$

$$p_y(y) = \exp(-y^2/2\sigma_y^2). \tag{8}$$

If we assume that the incident pulses are Gaussian shaped with a center frequency f_c and a 6 dB fractional bandwidth B, the characteristic width of the axial PSF component can be computed using

$$\sigma_z = \frac{c}{2\pi B f_c} = \frac{\lambda}{2\pi B}. \tag{9}$$

For 2D arrays, the beam widths along the lateral and elevational directions are determined by the effective transducer aperture D, the wavelength, and the depth, which can be approximated by

$$\sigma_x = \sigma_y = \frac{0.4 z_{01}\lambda}{D}. \tag{10}$$

The lateral, elevational, and axial distances from scatterers to the beam axis for the pre- and postdeformation cases can be written as

$$l_{1x} = x - x_0, \quad l_{1y} = y - y_0, \quad l_{1z} = z - z_{01},$$

$$l_{2x} = bx - x_0, \quad l_{2y} = by - y_0 \quad l_{2z} = az - z_{02}, \tag{11}$$

where z_{02} is the depth of the point of interest after deformation. We can then evaluate the integral in Eq. (4) along the axial, lateral, and elevational directions separately,

$$\langle s_1 s_2^* \rangle = I_x I_y I_z, \tag{12}$$

where I_x, I_y, and I_z are the absolute values of the integral along x, y, and z directions,

$$I_x = \left| \int \exp\left(-\frac{l_{1x}^2 + l_{2x}^2}{2\sigma_x^2}\right) \times \exp\left(j\frac{2\pi[(b^2-1)x^2 - 2(b-1)x_0 x]}{\lambda z_{01}}\right) dx \right|$$

$$= \sqrt{\frac{2\pi}{b^2+1}}\sigma_x \exp\left[-\frac{(b-1)^2 x_0^2}{2\sigma_x^2(b^2+1)}\right]. \tag{13}$$

Similarly we can obtain

$$I_y = \sqrt{\frac{2\pi}{b^2+1}}\sigma_y \exp\left[-\frac{(b-1)^2 y_0^2}{2\sigma_y^2(b^2+1)}\right], \tag{14}$$

$$I_z = \sqrt{\frac{2\pi}{a^2+1}}\sigma_z \exp\left[-\frac{(az_{01}-z_{02})^2}{2\sigma_z^2(a^2+1)} - \frac{(a^2-1)^2}{2B^2(a^2+1)}\right]. \tag{15}$$

The correlation coefficient can be computed as follows:

$$\rho = \frac{\langle s_1 s_2^* \rangle}{\sqrt{\langle s_1 s_1^* \rangle \langle s_2 s_2^* \rangle}}. \tag{16}$$

Substituting Eq. (12) into Eq. (16), we obtain

$$\rho = \rho_x \rho_y \rho_z, \tag{17}$$

where ρ_x, ρ_y, and ρ_z are the effective correlation coefficients along the lateral, elevational, and axial directions, respectively,

$$\rho_x = \sqrt{\frac{2b}{b^2+1}} \exp\left[-\frac{(b-1)^2 x_0^2}{2\sigma_x^2(b^2+1)}\right], \tag{18}$$

$$\rho_y = \sqrt{\frac{2b}{b^2+1}} \exp\left[-\frac{(b-1)^2 y_0^2}{2\sigma_y^2(b^2+1)}\right], \tag{19}$$

$$\rho_z = \sqrt{\frac{2a}{a^2+1}} \exp\left[-\frac{(az_{01}-z_{02})^2}{2\sigma_z^2(a^2+1)} - \frac{(a^2-1)^2}{2B^2(a^2+1)}\right]. \tag{20}$$

Equation (17) provides an expression for the correlation coefficient between the pre- and postdeformation signals acquired from the location of interest. For elastographic processing, finite gated segments of the echo signal are utilized. A gated data segment is generally selected using a rectangular window. Generally, the same window is used for both the pre- and postdeformation data segments. Attenuation and focusing effects can be included in the window function $w(t)$, such that the intensity of $s(t)$ can be considered to be constant with depth. Thus, the correlation coefficient between the pre- and postdeformation data segments can be computed using[18]

$$\rho_{1,2} = \frac{\int_{t_1}^{t_2} w^2(t)\langle s_1(t)s_2^*(t)\rangle/\bar{I}dt}{\int_{t_1}^{t_2} w^2(t)dt} = \frac{\int_{-Z/2}^{Z/2} w^2(\xi)\langle s_1(\xi)s_2^*(\xi)\rangle/\bar{I}d\xi}{\int_{-Z/2}^{Z/2} w^2(\xi)d\xi} = \frac{\int_{-Z/2}^{Z/2} w^2(\xi)\rho(\xi)d\xi}{\int_{-Z/2}^{Z/2} w^2(\xi)d\xi}, \tag{21}$$

where $\bar{I} = \langle ss^* \rangle$ is the mean signal intensity, Z is the window length of the windowed rf echo signal segment, and ξ is the distance from a position within the window to the center of the window, which is in the range from $-Z/2$ to $Z/2$. $\rho(\xi)$ is the correlation of signals resulting from position ξ within the window of the rf segment. To compute $\rho(\xi)$, we only need to change the value of z_{01} and z_{02} as

$$z_{01} = z_0 + \xi, \quad z_{02} = az_0 + \xi, \tag{22}$$

where z_0 is the depth of the rf segment center. Substituting Eq. (22) into Eq. (20), and then plugging the result into Eq. (17), we can obtain $\rho(\xi)$.

III. SIMULATION

A. Method

A uniformly elastic simulated TM phantom and a single inclusion phantom with dimensions $4\times4\times4$ cm^3 was utilized to evaluate the signal decorrelation due to deformation. Both phantoms were constructed using the FEA software (ANSYS Inc., Canonsburg, USA), with a Poisson's ratio of 0.495 assumed for both the inclusion and the background. The inclusion phantom contains a 1 cm diameter spherical inclusion, which was three times stiffer than the background. To apply a uniaxial deformation, the simulated phantoms were fixed on the top surface and a displacement load (in the z direction) was applied to the bottom surface. Tissue displacement in the lateral and elevational direction were unconstrained. The local displacement due to the applied deformation was then estimated by solving the associated partial differential equations numerically.

The FEA displacement field was then utilized in an ultrasound simulation program[19,20] to generate pre- and postdeformation rf echo signal data for elastographic processing. This program simulates the frequency domain response of ultrasound wave propagating through a scattering medium. The frequency response is then transformed back to the time domain to obtain ultrasound radio frequency frames. This simulation program achieves similar rf waveforms when compared to typical time domain simulation programs such as FIELD II.[21] Modern beam forming techniques such as apodization, dynamic aperture, dynamic receive focusing, and 3D beam steering can also be simulated with our simulation program.[20] The accuracy of the frequency domain simulation model has also been assessed in our previous work[20] by comparing it with FIELD II. In our simulation, a numerical phantom was constructed with scatterers modeled using 50 μm radius glass beads, which were randomly distributed in the phantom at a number density of 10 scatterers/mm^3 to ensure Rayleigh scattering.[16] The 3D displacement fields from ANSYS, after appropriate interpolation to a regular Cartesian grid, were used to displace the scatterers and generate the deformed phantom to generate the postdeformation signals.

A 1D linear array was modeled, which consisted of 64 elements with dimensions of 150 μm$\times$12 mm and center-to-center spacing of 0.2 mm. This configuration produces a lateral aperture size around 12.8 mm. The elevational focus was set at 50 mm and the lateral transmit focus at 30 mm. Dynamic receive focusing was also utilized with an F-number set at 2. Simulated 2D array transducers having 32×32 and 64×64 active elements were also modeled with square elements of size 0.15 mm with a 0.2 mm center-to-center element separation. Hence, the aperture size is around 6.4 and 12.8 mm for 32×32 and 64×64 2D arrays, respectively. We used a single transmit focus at 30 mm and dynamic receive focus with an F-number set at 2 for both the lateral and elevational directions. The incident pulses were modeled to be Gaussian shaped with a 6 MHz center frequency and a 60% bandwidth. The simulations were performed assuming that the sound speed in the phantom was constant at 1540 m/s and negligible attenuation. The sampling frequency utilized was 52 MHz. For a $4\times4\times4$ cm^3 simulated phantom, 200 elevational slices were generated. In each elevational slice, 400 A-lines were simulated in the lateral direction. So a total of 80 000 (400×200) A-lines were acquired in one single 3D scan.

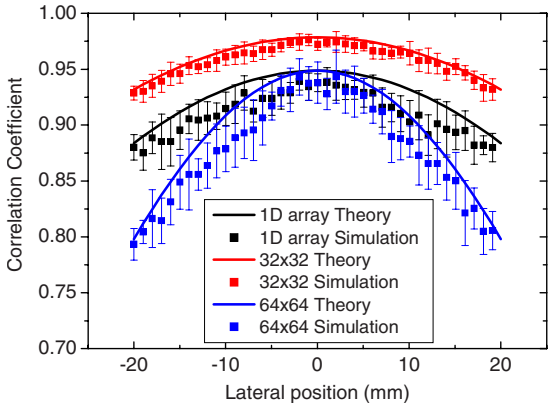

FIG. 1. (Color online) Comparison between theoretical prediction and simulation results for the correlation coefficient of pre- and postcompression rf segments as a function of the lateral position. Results are shown for (a) 1D array and (b) 32×32 and (c) 64×64 2D transducer arrays. The applied strain was 2%.

B. Results

Theoretical results demonstrating the variation in the correlation coefficient are verified using simulated rf data obtained using a uniformly elastic phantom. Figure 1 shows a comparison between the theoretical prediction and simulation results for the correlation coefficient of pre- and postdeformation rf segments as a function of lateral position. Results obtained using the 1D array and 32×32 and 64×64 2D array transducers are presented. The correlation coefficient was obtained using a 3 mm rf data segment centered at a depth of 3 cm from the transducer and at an elevational distance of 1 cm from the axis of symmetry of the elevational displacement field. The applied strain was 2%. The simulation results for the normalized correlation coefficient are measured using cross-correlation techniques applied to data segment from pre- and postdeformation rf A-lines. The error bars denote the standard deviation of the mean correlation coefficient estimates over 12 independent data sets, which were obtained using 12 independent realizations of the ultrasound simulation program with randomly distributed tissue scatterers. For the 1D array, we assume that the beam profile has a Gaussian shape in the elevational direction as well. To predict the correlation coefficient, the beam width used in Eq. (8) was obtained by measuring the simulated ultrasound beam profiles.

As illustrated in the figure, the correlation coefficient decreases with an increase in the lateral position moving from the center to the edge of the phantom. This is due to the increased scatterer motion or displacement across the beam at the edges of the phantom when compared to the motion or displacement at the center. Note that the correlation coefficient decreases faster for the 64×64 2D array when compared to the 1D array and 32×32 array. This difference is due to the different aperture sizes utilized for the three simu-

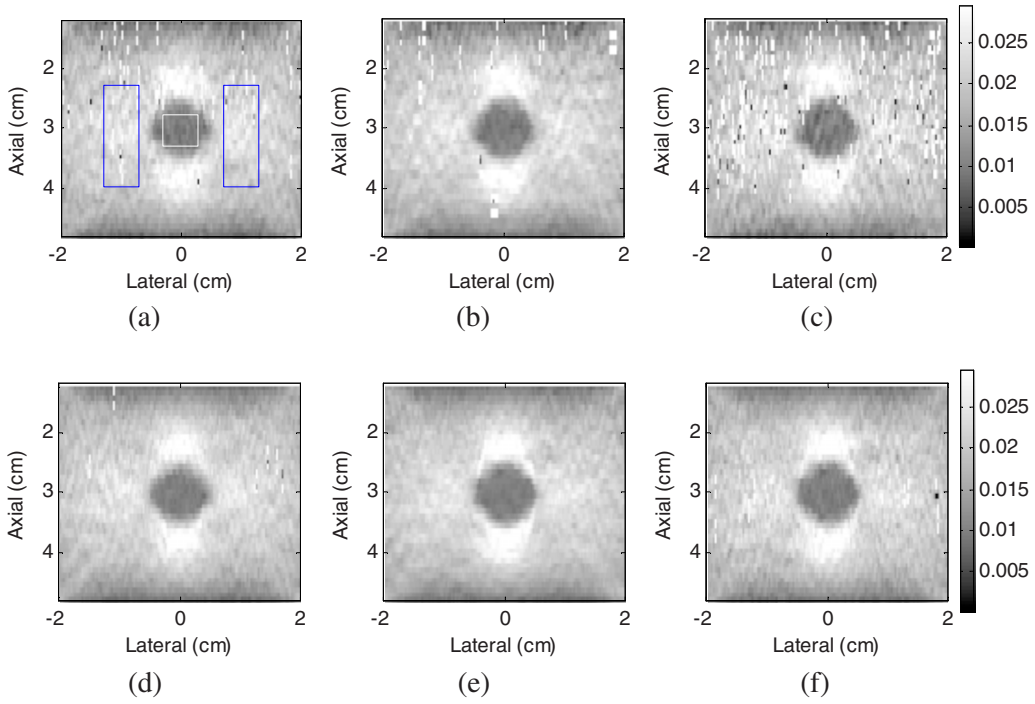

FIG. 2. (Color online) Simulated axial strain images of a spherical inclusion phantom obtained using [(a) and (d)] 1D array [(b) and (e)] 32×32 and [(c) and (f)] 64×64 2D arrays. The first row presents strain images obtained using 2D motion tracking algorithm without motion compensation in the elevational direction, and the second row depicts strain images obtained using 3D motion tracking algorithm. The center frequency is 4 MHz.

lated cases. Larger aperture sizes produce narrower beams and thereby induce faster signal decorrelation.

Furthermore, it can be observed in Fig. 1 that the theoretical predictions of the correlation coefficient are slightly higher than the simulation results. This is because our theoretical model assumes that the displacement along the axial direction has been accurately tracked, in which case the correlation coefficient achieves the maximum value at that position. The simulation results, however, inevitably contain errors in the displacement estimates due to the motion tracking algorithm and sampling precision. Therefore, the correlation coefficient obtained from simulation is generally lower than that from theoretical prediction.

Figure 2 presents simulated strain images of the spherical inclusion phantom obtained using the 1D array [(a) and (d)] and 32×32 [(b) and (e)] and 64×64 [(c) and (f)] 2D arrays. The first row illustrates strain images obtained using 2D motion tracking algorithm without motion compensation in the elevational direction, and the second row depicts strain images obtained using a 3D motion tracking algorithm. In this study, we used a 1D kernel, which is approximately 3 mm in the axial direction and one *A*-line along the lateral direction, to compute the cross-correlation function and to determine the displacement. A three-point, least squares strain estimator[22] was then used to generate local strain estimates. To better visualize the decorrelation noise in the strain images, median filters were not used for the displacement and strain estimated. It is assumed that the spherical inclusion is centered at a depth of 3 cm from the transducer and a distance of 1.5 cm from the elevational axis (y_0=1.5 cm). The applied strain is 2%, and the center frequency is 4 MHz with a 60% bandwidth. As expected, the decorrelation noise has been reduced after elevational motion compensation. The strain images obtained using the 64×64 2D array are more sensitive to signal decorrelation due to elevational motion. This is because the ultrasound beam produced by the 64×64 array is narrower along both the lateral and elevational directions. The noise performance of the 1D array is similar to that of the 32×32 2D array, but the inclusion looks smaller in the strain images [Figs. 2(a) and 2(d)] due to the poor slice thickness performance. In this example, the 32×32 2D array is the best choice for strain estimation as it provides good performance in terms of the noise level and spatial resolution.

Figure 3 compares the SNR_e and CNR_e of the simulated axial strain images of the inclusion phantom obtained using the 1D array and 32×32 and 64×64 2D arrays shown in Fig. 2. The quantitative SNR_e and CNR_e parameters were calculated using a rectangular region of interest (ROI) within the inclusion and in the background region, as shown in Fig. 2(a). Note that the image quality is significantly improved using the 3D motion tracking algorithm, especially for the 64×64 2D array.

Figure 4 presents simulated axial strain images of the inclusion phantom obtained using 32×32 (left) and 64×64 (right) 2D arrays shown in the lateral-elevation plane at a depth of 3 cm. It is assumed that the spherical inclusion is centered at a depth of 3 cm from the transducer and on the elevational axis (y_0=0 cm). Observe the decreased decorrelation noise at the elevational edges of the phantom obtained using the 3D motion tracking algorithm, especially for the 64×64 2D array.

To illustrate the impact of the center frequency, simulated axial strain images of the inclusion phantom were obtained using center frequencies of 6, 8, and 10 MHz for a 32×32 2D array, as shown in Fig. 5. Results obtained by

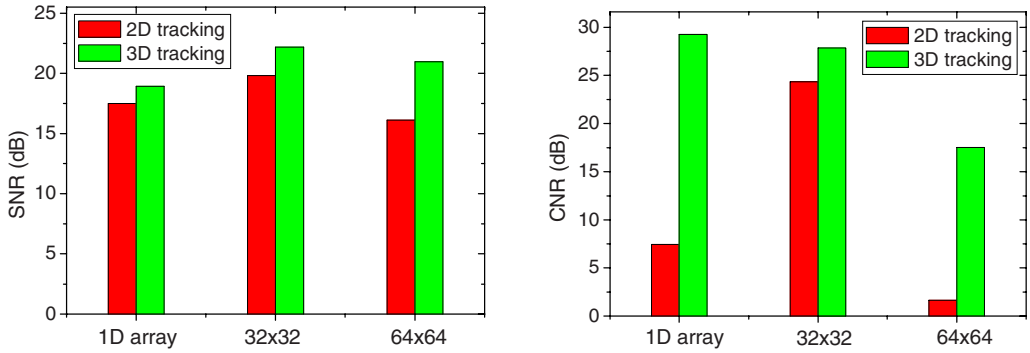

FIG. 3. (Color online) A bar graph of the signal-to-noise (SNR) and contrast-to-noise (CNR) values of the simulated axial strain images of the inclusion phantom obtained using 1D array and 32×32 and 64×64 2D arrays shown in Fig. 2.

applying a compression or deformation of 1% (top) and 2% (bottom) were compared using a 3D motion tracking algorithm. All the other simulation parameters were the same as those described in Fig. 4. As expected, increased decorrelation noise artifacts are observed when higher frequencies and larger deformations are used.

IV. DISCUSSION

2D array transducers represent a promising solution for the implementation of volume data acquisition for real time 3D strain imaging. The effective aperture size is an important parameter for 2D array systems since it determines the number of elements required for a given element size and spacing between adjacent elements. It is desirable to use a small number of active elements to obtain good strain images. Generally, larger apertures provide an improved ultrasound resolution but introduce increased decorrelation noise artifacts due to the narrower beam width. We need to take into consideration this tradeoff when choosing the aperture size of the 2D transducer array for strain imaging. Therefore, it is useful to understand how the aperture size and other system factors affect the correlation between pre- and postdeformation signals.

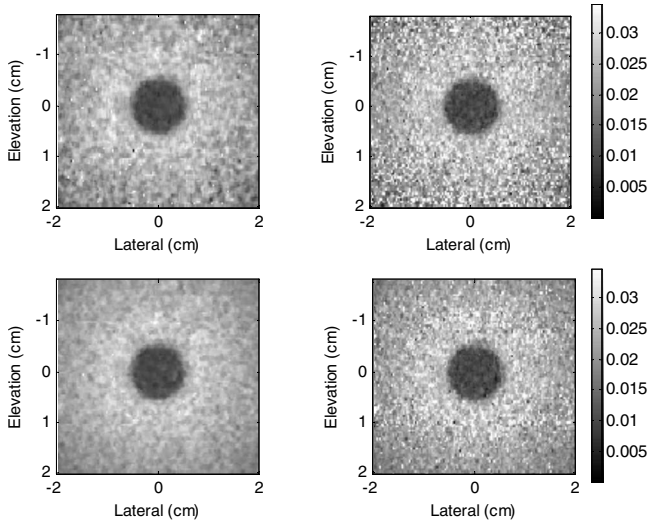

FIG. 4. Simulated axial strain images of the inclusion phantom obtained using 32×32 (left) and 64×64 (right) 2D arrays shown in the lateral-elevation plane at depth 3 cm. The first row presents strain images obtained using 2D motion tracking algorithm, and the second row depicts strain images obtained using 3D motion tracking algorithm. The center frequency is 4 MHz.

Figure 6 presents theoretical correlation coefficient curves as a function of the aperture size of a 2D array for different applied strains. The center frequency is 6 MHz and the fractional bandwidth is 60%. Results are obtained using 3 mm rf segments centered at a depth of 3 cm, in the center along the lateral direction and 1 cm from the center in the elevational direction (x_0=0 cm; y_0=1 cm). As illustrated in the figure, the decorrelation rate of the rf signal pairs increases with the value of the applied strain. This increased decorrelation rate is due to the fact that with increased strain more scatterers would leave the beam, leading to increased decorrelation, especially for larger aperture sizes.

Figure 7 shows the theoretical prediction of the correlation coefficient versus the 2D array aperture size for different center frequencies. We assume a fractional bandwidth of 60% for all the cases. Results are obtained using 3 mm rf segments centered at a depth of 3 cm, in the center along the lateral direction and 1 cm from the center in the elevational direction (x_0=0 cm; y_0=1 cm). The applied strain is 2%. As illustrated in the figure, the signal decorrelation rate of the rf signal pairs increases with the center frequency. This is primarily due to the fact that the ultrasound beam becomes narrower with the increased center frequency, enabling scatterers that are within the predeformation beam to leave the beam and newer scatterers to come within the beam after deformation when the beam becomes narrower, especially for larger aperture sizes.

Figure 8 shows the theoretical prediction of the correlation coefficient versus the 2D array aperture size for rf signals obtained at different elevational positions. Results are obtained using 3 mm rf segments centered at a depth of 3 cm, in the center along the lateral direction (x_0=0 cm). The applied strain is 2% and the center frequency is 6 MHz. As expected, the signal decorrelation rate is larger at the edges of the target, where the elevational motion is the largest. Signals obtained using larger aperture sizes are more sensitive to decorrelation caused by the elevational motion since the beam is narrower for the larger apertures. Note that the correlation coefficient is independent of the aperture size

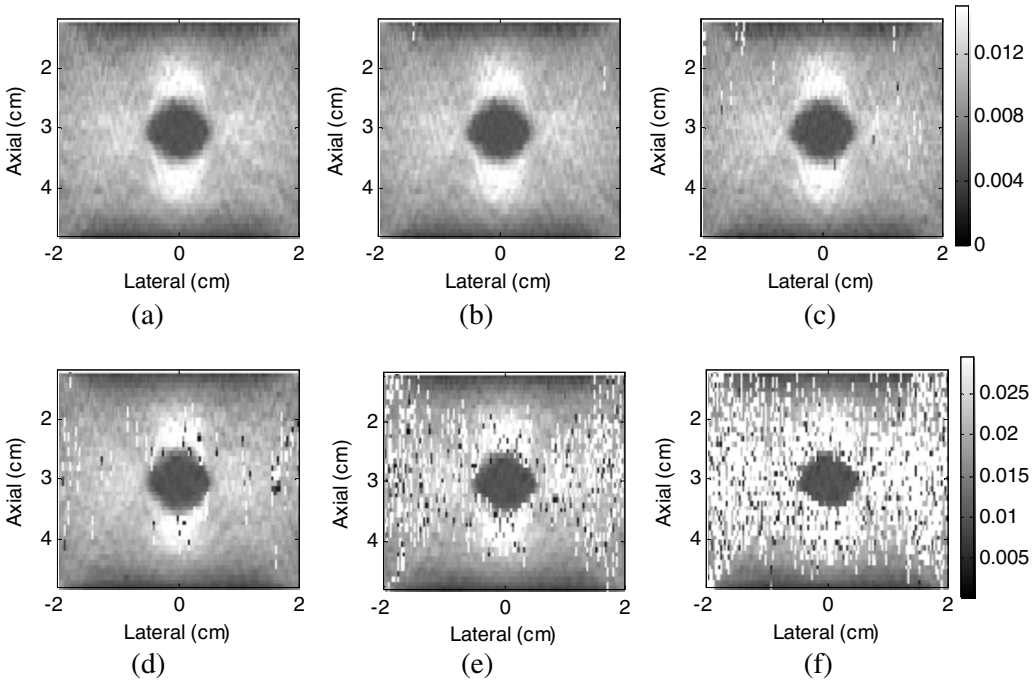

FIG. 5. Simulated axial strain images of the inclusion phantom obtained using the center frequency of [(a) and (d)] 6 MHz, [(b) and (e)] 8 MHz, and [(c) and (f)] 10 MHz for the 32×32 2D array. The applied strain is 1% (top) and 2% (bottom).

for rf signals obtained at the geometric center of the target, where the motion of tissue scatterers in the lateral and elevational directions is the smallest.

Figure 9 shows the theoretical prediction of the correlation coefficient versus the 2D array aperture size for rf signals obtained at different depths. Results are obtained using 3 mm rf segments in the center along the lateral direction and 1 cm from the center in the elevational direction (x_0 =0 cm; y_0=1 cm). The applied strain is 2% and the center frequency is 6 MHz. As illustrated in the figure, the signal decorrelation rate for the rf signal is higher at shallow depths. This is because at shallow depths the phase changes ($\Delta\phi$) are larger due to the motion of scatterers in the lateral and elevational directions. Note that our model estimates the correlation coefficient of rf segments after axial motion compensation. Thus, the correlation coefficient is higher regardless of the large axial displacement at deeper depths.

V. CONCLUSIONS

In this paper, we investigate the impact of decorrelation noise in strain imaging, resulting from the motion of tissue scatterers in all three dimensions. Under the assumption that the system PSF is separable, as shown in Eq. (7), a theoretical expression has been derived for the signal decorrelation between pre- and postdeformation rf echo signals. The theoretical prediction matches well with the simulation results. Simulated axial strain images of a spherical inclusion phantom obtained using both 1D and 2D array transducers are

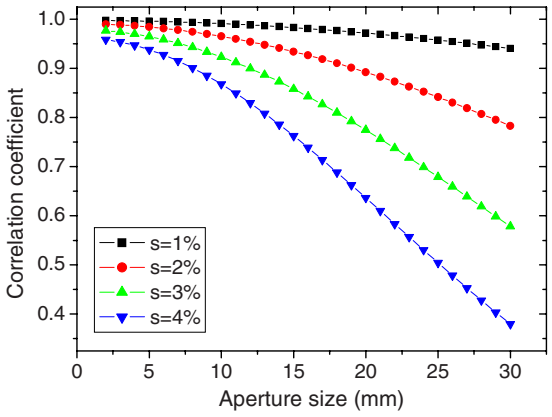

FIG. 6. (Color online) Plots of the theoretical prediction of the correlation coefficient vs the 2D array aperture size for different applied strains. Results are obtained using 3 mm rf segments centered at a depth of 3 cm, in the center along the lateral direction and 1 cm from the center in the elevational direction (x_0=0 cm; y_0=1 cm). The center frequency is 6 MHz.

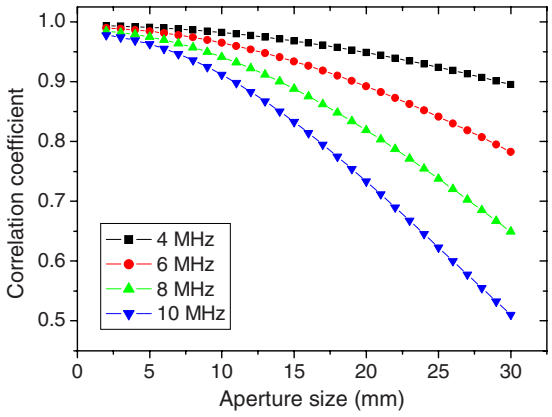

FIG. 7. (Color online) Plots of the theoretical prediction of the correlation coefficient vs the 2D array aperture size for different center frequencies. Results are obtained using 3 mm rf segments centered at a depth of 3 cm, in the center along the lateral direction and 1 cm from the center in the elevational direction (x_0=0 cm; y_0=1 cm). The applied strain is 2%.

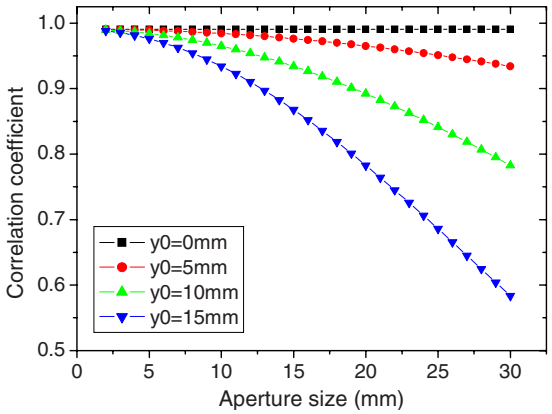

FIG. 8. (Color online) Plots of the theoretical prediction of the correlation coefficient vs the 2D array aperture size for rf signals obtained at different elevational positions. Results are obtained using 3 mm rf segments centered at a depth of 3 cm, in the center along the lateral direction (x_0=0 cm). The applied strain is 2% and the center frequency is 6 MHz.

also presented. A quantitative comparison of the image quality of strain images obtained using different motion tracking algorithms demonstrates that 3D motion tracking is necessary for imaging systems using 2D array transducers. For 3D real time strain imaging, the theoretical derivation presented in this paper would enable the estimation of optimal parameters, such as the aperture size, center frequency, and applied strain. To detect stiffer lesions at shallow depths, a 2D transducer array with a smaller effective aperture is a good choice since it provides high resolution and low decorrelation noise, and at the same time, fewer elements are required for a given spacing between elements.

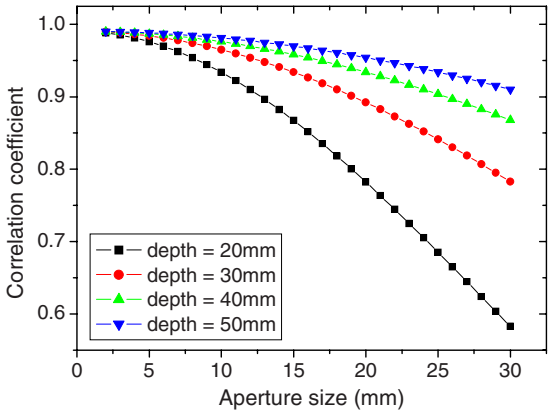

FIG. 9. (Color online) Plots of the theoretical prediction of the correlation coefficient vs the 2D array aperture size for rf signals obtained at different depths. Results are obtained using 3 mm rf segments in the center along the lateral direction and 1 cm from the center in the elevational direction (x_0 =0 cm; y_0=1 cm). The applied strain is 2% and the center frequency is 6 MHz.

[1]Y. G. Fung, *Biomechanical Properties of Living Tissues* (Springer, New York, 1981).
[2]J. S. Jurvelin, M. D. Buschmann, and E. B. B. Hunziker, "Mechanical anisotropy of the human knee articular cartilage in compression," Proc. Inst. Mech. Eng., Part H: J. Eng. Med. **217**, 215–219 (2003).
[3]E. E. Konofagou, T. P. Harrigan, J. Ophir, and T. A. Krouskop, "Poroelastography: Imaging the poroelastic properties of tissues," Ultrasound Med. Biol. **27**, 1387–1397 (2001).
[4]R. Righetti, J. Ophir, S. Srinivasan, and T. A. Krouskop, "The feasibility of using elastography for imaging the Poisson's ratio in porous media," Ultrasound Med. Biol. **30**(2), 215–228 (2004).
[5]F. Kallel and J. Ophir, "Three-dimensional tissue motion and its effect on image noise in elastography," IEEE Trans. Ultrason. Ferroelectr. Freq. Control **44**, 1286–1296 (1997).
[6]M. Bilgen, "Dynamics of errors in 3D motion estimation and implications for strain-tenser imaging in acoustic elastography," Phys. Med. Biol. **45**, 1565–1578 (2000).
[7]M. Odonnell, A. R. Skovoroda, B. M. Shapo, and S. Y. Emelianov, "Internal displacement and strain imaging using ultrasonic speckle tracking," IEEE Trans. Ultrason. Ferroelectr. Freq. Control **41**, 314–325 (1994).
[8]F. Kallel and M. Bertrand, "Tissue elasticity reconstruction using linear perturbation method," IEEE Trans. Med. Imaging **15**, 299–313 (1996).
[9]E. E. Konofagou and J. Ophir, "Precision estimation and imaging of normal and shear components of the 3D strain tensor in elastography," Phys. Med. Biol. **45**, 1553–1563 (2000).
[10]J. E. Lindop, M. T. Graham, A. H. Gee, and R. W. Prager, "3D elastography using freehand ultrasound," Ultrasound Med. Biol. **32**, 529–545 (2006).
[11]S. I. Awad and J. T. Yen, "3D strain imaging using a rectilinear 2D array," Ultrason. Imaging **29**, 220–230 (2007).
[12]A. V. Patil, C. D. Garson, and J. A. Hossack, "3D prostate elastography: algorithm, simulations and experiments," Phys. Med. Biol. **52**, 3643–3663 (2007).
[13]G. Said, O. Basset, J. M. Mari, C. Cachard, E. Brusseau, and D. Vray, "Experimental three dimensional strain estimation from ultrasonic sectorial data," Ultrasonics **44**, E189–E193 (2006).
[14]J. Meunier and M. Bertrand, "Ultrasonic texture motion analysis—Theory and simulation," IEEE Trans. Med. Imaging **14**, 293–300 (1995).
[15]R. F. Wagner, M. F. Insana, and S. W. Smith, "Fundamental correlation lengths of coherent speckle in medical ultrasonic images," IEEE Trans. Ultrason. Ferroelectr. Freq. Control **35**, 34–44 (1988).
[16]R. F. Wagner, S. W. Smith, J. M. Sandrik, and H. Lopez, "Statistics of speckle in ultrasound B-scans," IEEE Trans. Sonics Ultrason. **30**, 156–163 (1983).
[17]M. Rao and T. Varghese, "Correlation analysis of the beam angle dependence for elastography," J. Acoust. Soc. Am. **119**, 4093–4101 (2006).
[18]Q. Chen, A. L. Gerig, U. Techavipoo, J. Zagzebski, and T. Varghese, "Correlation of RF signals during angular compounding," IEEE Trans. Ultrason. Ferroelectr. Freq. Control **52**, 961–970 (2005).
[19]Y. D. Li and J. A. Zagzebski, "A frequency domain model for generating B-mode images with array transducers," IEEE Trans. Ultrason. Ferroelectr. Freq. Control **46**, 690–699 (1999).
[20]M. Rao, T. Varghese, and J. Zagzebski, "Simulation of ultrasound two-dimensional array transducers using a frequency domain model," Med. Phys. **35**, 3162–3169 (2008).
[21]J. A. Jensen and N. B. Svendsen, "Calculation of pressure fields from arbitrarily shaped, apodized and excited ultrasound transducers," IEEE Trans. Ultrason. Ferroelectr. Freq. Control **39**, 262–267 (1992).
[22]F. Kallel and J. Ophir, "A least-squares strain estimator for elastography," Ultrason. Imaging **19**, 195–208 (1997).